Thermohaline structure in the California Current System: Observations and modeling of spice variance

Robert E. Todd,[1] Daniel L. Rudnick,[2] Matthew R. Mazloff,[2] Bruce D. Cornuelle,[2] and Russ E. Davis[2]

[1]   Upper ocean thermohaline structure in the California Current System is investigated using sustained observations from autonomous underwater gliders and a numerical state estimate. Both observations and the state estimate show layers distinguished by the temperature and salinity variability along isopycnals (i.e., spice variance). Mesoscale and submesoscale spice variance is largest in the remnant mixed layer, decreases to a minimum below the pycnocline near 26.3 kg m^{-3}, and then increases again near 26.6 kg m^{-3}. Layers of high (low) meso- and submesoscale spice variance are found on isopycnals where large-scale spice gradients are large (small), consistent with stirring of large-scale gradients to produce smaller scale thermohaline structure. Passive tracer adjoint calculations in the state estimate are used to investigate possible mechanisms for the formation of the layers of spice variance. Layers of high spice variance are found to have distinct origins and to be associated with named water masses; high spice variance water in the remnant mixed layer has northerly origin and is identified as Pacific Subarctic water, while the water in the deeper high spice variance layer has southerly origin and is identified as Equatorial Pacific water. The layer of low spice variance near 26.3 kg m^{-3} lies between the named water masses and does not have a clear origin. Both effective horizontal diffusivity, κ_h, and effective diapycnal diffusivity, κ_v, are elevated relative to the diffusion coefficients set in the numerical simulation, but changes in κ_h and κ_v with depth are not sufficient to explain the observed layering of thermohaline structure.

1. Introduction

[2]   Temperature and salinity structure in the California Current System (CCS) is the end result of stirring and mixing of different water masses across a range of scales. In this eastern boundary current system, the equatorward flowing California Current carries cool, fresh Pacific Subarctic water southward while persistent poleward flows carry warm, salty Equatorial Pacific water northward [*Hickey*, 1979; *Lynn and Simpson*, 1987, 1990; *Todd et al.*, 2011a]. These water masses meet in a region with vigorous eddy activity [*Davis et al.*, 2008; *Todd et al.*, 2009] and upwelling [*Davis*, 2010; *Song et al.*, 2011] that contribute meso- and submesoscale structure. Long-term observations by underwater gliders in the CCS resolve the resulting thermohaline structure and reveal along-isopycnal layers that are distinguished by temperature and salinity variance along isopycnals (i.e., spice variance).

We investigate the history of water in these layers using passive tracers in a numerical state estimate.

[3]   Upper ocean thermohaline structure may be studied by examining temperature and salinity along isobaric or isopycnal surfaces. Along surfaces of constant depth, heaving by internal waves causes vertical stratification to be projected onto the horizontal through tilting of isopycnals. Thermohaline variability along isopycnals is unaffected by the internal wave field and variability is controlled by horizontal advection and diapycnal mixing [*Ferrari and Polzin*, 2005; *Cole and Rudnick*, 2012]. Temperature and salinity fluctuations along isopycnals, which vary from cold and fresh to warm and salty, provide a dynamically passive tracer [*Veronis*, 1972] that has been referred to as spice [*Munk*, 1981].

[4]   Layers distinguished by spice variance have been observed previously, and their existence has been attributed to a variety of processes. In the North Atlantic, the outflow of Mediterranean Water at depths of 900–1400 m creates a large-scale spice gradient that is stirred to produce a mid-depth layer of enhanced spice variance [*Ferrari and Polzin*, 2005]. Using 2.5 years of repeated glider transects in the North Pacific, *Cole and Rudnick* [2012] showed that elevated spice variance along certain isopycnals was the result of water properties set at the surface before subduction and diapycnal mixing between water masses.

[1]Woods Hole Oceanographic Institution, Woods Hole, Massachusetts, USA.
[2]Scripps Institution of Oceanography, University of California, San Diego, La Jolla, California, USA.
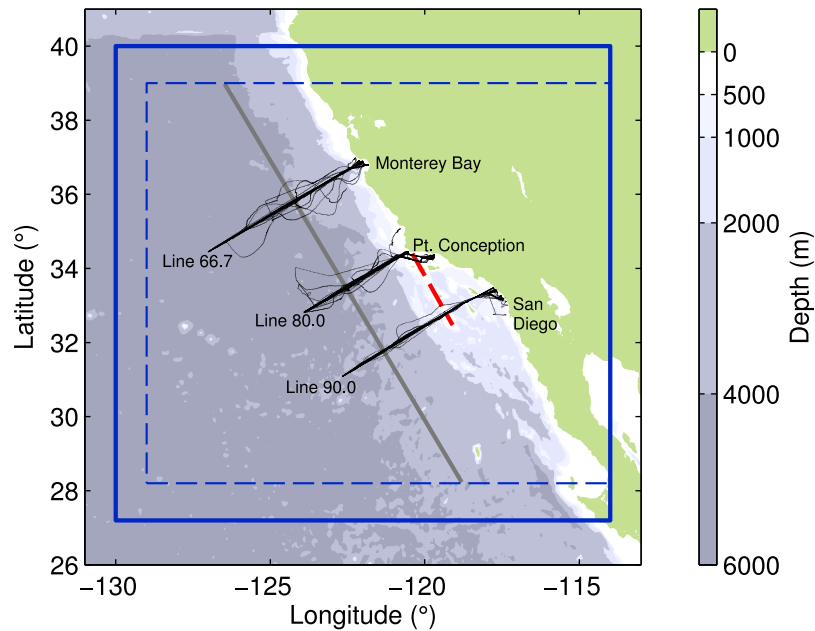
Figure 1. Tracks of all glider deployments along CalCOFI Lines 66.7, 80.0, and 90.0 (black) with bathymetry in color. The blue box denotes the full domain of the numerical simulation, and the dashed blue box denotes the cropped portion of the model domain used for analysis. The grey line shows the alongshore transect examined in the simulation. The dashed red line denotes the Santa Rosa Ridge, which is the offshore boundary of the Southern California Bight.

[5] Underwater gliders [*Davis et al.*, 2002; *Rudnick et al.*, 2004] are well-suited for providing long-term observations of thermohaline structure in the upper ocean. Gliders can provide a continuous presence that would be prohibitively expensive using ship-based observational tools while collecting measurements at high spatial resolution (typically a few kilometers between profiles). In many parts of the ocean, gliders are able to occupy predefined transects repeatedly with relatively small current-induced deviations [e.g., *Perry et al.*, 2008; *Castelao et al.*, 2010; *Todd et al.*, 2011a; *Cole and Rudnick*, 2012].

[6] Numerical state estimation [*Wunsch*, 2006; *Wunsch and Heimbach*, 2007] is a powerful tool for understanding oceanic processes. A 'state estimate' is a dynamically consistent numerical simulation with controls (e.g., forcing, initial conditions, and boundary conditions) adjusted so that the simulation agrees well with a wide array of observations over an extended period of time [*Wunsch and Heimbach*, 2007]. *Todd et al.* [2011a] showed that a numerical state estimate of the CCS that incorporates observations from gliders and other sources reproduces the velocity field in the region well. In this analysis, we take advantage of the adjoint model [*Heimbach et al.*, 2005] of the same simulation to investigate the past distributions of tagged waters.

[7] This paper is organized as follows: section 2 describes our glider observations, numerical state estimate, and analysis techniques; section 3.1 describes the mean, large-scale thermohaline structure in the CCS; section 3.2 describes layers defined by mesoscale and submesoscale spice variance; section 3.3 considers the history of those layers using passive tracer adjoint calculations in the numerical state estimate; and section 4 summarizes the results. Appendix A derives both the adjoint to the advection-diffusion equation

governing a passive tracer and the passive tracer sensitivity in a continuous framework.

2. Data and Methods

2.1. Glider Observations

[8] Spray gliders [*Sherman et al.*, 2001; *Rudnick et al.*, 2004] have been continually surveying in the CCS [*Davis et al.*, 2008; *Todd et al.*, 2011a, 2011b] along California Cooperative Oceanic Fisheries Investigations (CalCOFI) Lines 66.7, 80.0, and 90.0 (Figure 1) for more than 4 years. Line 66.7 extends about 525 km southwestward from Monterey Bay; Line 80.0 extends about 375 km southwestward from Point Conception; and Line 90.0 extends about 525 km southwestward from Dana Point, California and through the Southern California Bight (SCB). Continuous observations along Lines 80.0 and 90.0 began in October 2006, while glider surveys along Line 66.7 began in April 2007 (Figures 2a–2c). Gliders provide observations of temperature, salinity, density, velocity, chlorophyll fluorescence, and acoustic backscatter in the upper 500 m with horizontal resolution of about 3 km and transects repeated about every three weeks [*Davis et al.*, 2008; *Todd et al.*, 2011a, 2011b]. This analysis uses observations collected through October 2010 with a total of 40 transects on Line 66.7, 75 transects on Line 80.0, and 54 transects on Line 90.0. With the exception of February and March along Line 66.7, glider observations are well-spaced throughout the year on each line (Figures 2d–2f), so means calculated from the observations are not biased by the sampling pattern.

[9] Individual transects of salinity and density from each survey line (Figures 3a–3c) demonstrate the high spatial resolution of the glider observations and reveal variability
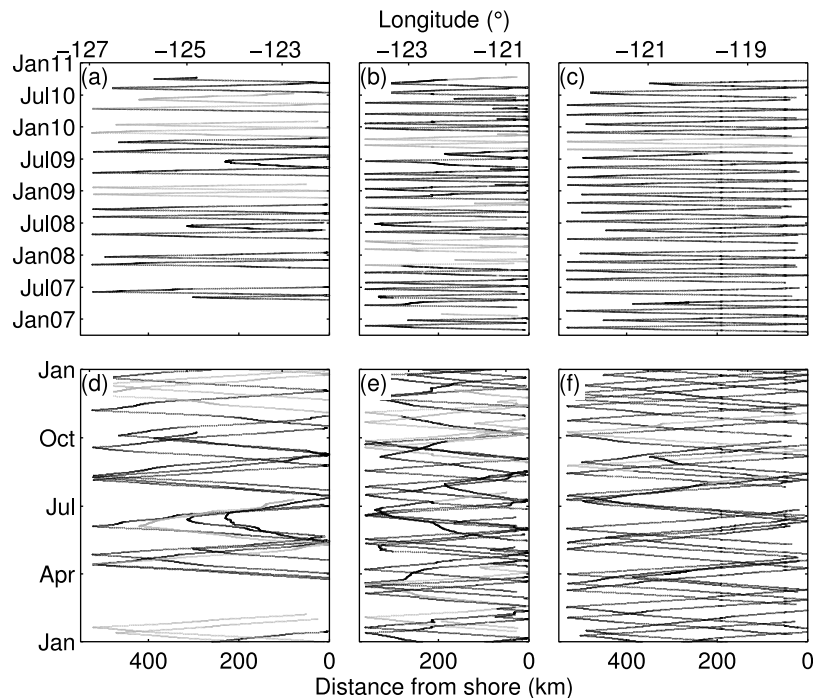
Figure 2. Across-shore and temporal sampling patterns along CalCOFI Lines (a, d) 66.7, (b, e) 80.0, and (c, f) 90.0. In Figures 2d–2f, the sampling pattern is plotted versus time of year to highlight coverage at seasonal scales. Each point denotes the location of a glider profile. Black points indicate profiles with valid ADP-derived current estimates; profiles without ADP-derived current estimates are grey. Tick marks on the upper axis of each panel indicate longitude while tick marks on the lower axes indicate distance from shore.

across all observed scales. The smallest-scale variability in isopycnal depth is largely due to heaving by the internal wave field. The relatively slow horizontal speed of the gliders (about 0.25 m s^{-1}) results in high-frequency temporal variability being aliased with high-wavenumber spatial variability [*Rudnick and Cole*, 2011], so much of the small-scale salinity variability in Figures 3a–3c is due to the vertical displacement of isopycnals. This effect is apparent in observations of properties along isobaric surfaces at scales smaller than about 30 km in the glider observations used here and in the observations of *Rudnick and Cole* [2011]; observations of properties along isopycnals are not affected because following isopycnals explicitly filters out internal waves [*Rudnick and Cole*, 2011].
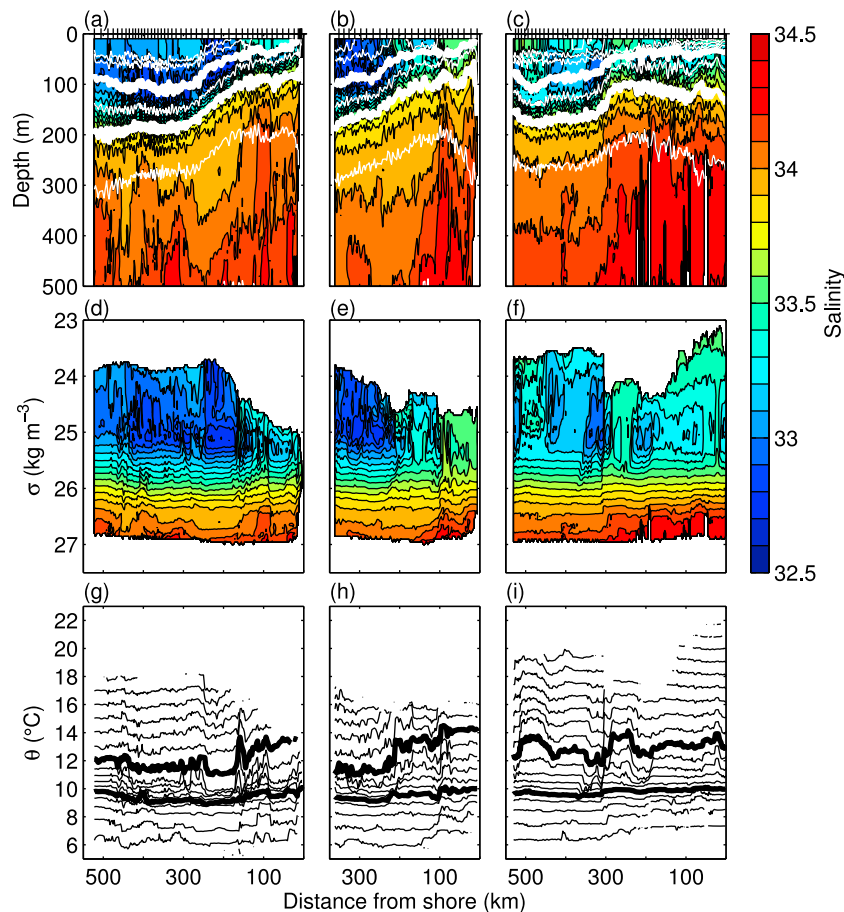
[10] Salinity (Figures 3d–3f) and potential temperature (Figures 3g–3i) along isopycnals also show variability across the range of observed scales. Along an isopycnal, fluctuations of potential temperature ($\Delta\theta$) and salinity (ΔS) are perfectly compensated, so $\alpha\Delta\theta = \beta\Delta S$, where α and β are the thermal and saline expansion coefficients, respectively. Therefore salinity along isopycnals and potential temperature along isopycnals exhibit the same variability. In Figures 3d–3i, wherever salinity increases (decreases) along an isopycnal there is a corresponding increase (decrease) in potential temperature along the same isopycnal; the presentation in Figures 3g–3i makes the relative magnitude of these spice fluctuations clearer since it does not rely on the choice of color scales. On some isopycnals, such as the 25.0 kg m^{-3} isopycnal on all three transects, spice fluctuations are

relatively large. Along the 26.0 kg m^{-3} isopycnal, spice fluctuations are noticeably smaller. Deeper still, spice fluctuations on these example transects increase again. This apparent layering of spice variability is the main focus of this analysis, and, as with *Cole and Rudnick* [2012], we choose along-isopycnal salinity to represent spice for the remainder of the analysis.

[11] As with *Todd et al.* [2011a], we create mean transects by objectively mapping observations from individual transects onto a uniform grid using a Gaussian covariance with a 30-km length scale, then averaging across transects. Mapping is performed along both depth surfaces and isopycnals. Alongshore geostrophic velocities, when used in place of missing Doppler-derived currents (Figure 2), are also calculated by objective mapping [*Todd et al.*, 2011a].

2.2. Numerical State Estimate

[12] The numerical state estimate used in this analysis is the same regional, data-assimilating version of the MITgcm [*Marshall et al.*, 1997a, 1997b] used by *Todd et al.* [2011a]. The model domain is [130°W 140°W] $\times$ [27.2°N 40°N] (Figure 1, solid blue box), and the period of simulation is 1 January 2007 to 30 July 2009. Here we use the 90th data-assimilating iteration. Open boundary conditions have not yet converged to optimal values, resulting in some unrealistic characteristics along the open boundaries. To avoid these areas, we restrict our analysis to the portion of the domain greater than 1° from the open boundaries (Figure 1, dashed blue box).

Figure 3. Example transects of (a–c) salinity (colors) and density (white contours) as a function of depth, (d–f) salinity as a function of density, and (g–i) potential temperature along isopycnals on Line 66.7 (Figures 3a, 3d, and 3g), Line 80.0 (Figures 3b, 3e, and 3h), and Line 90.0 (Figures 3c, 3f, and 3i). The 25.0 and 26.0 kg m^{-3} isopycnals are shown bold in Figures 3a–3c and Figures 3g–3i. Tick marks on the uppermost axes denote the locations of glider profiles; only every fifth profile location is shown for clarity.

2.3. Wavelets

[13] We use the wavelet transform to partition along-isopycnal salinity variance by scale and location. The wavelet transform, $\tilde{p}(s, x_0)$ [*Torrence and Compo*, 1998; *Ferrari and Rudnick*, 2000], of a variable $p(x)$ at scale s centered about location x_0 is

$$\tilde{p}(s, x_0) = \int_{-\infty}^{\infty} p(x)\psi_{s,x_0}^*(x)dx, \qquad (1)$$

where the ψ_{s,x_0} is a scaled and translated version of the mother wavelet, $\psi(x)$, given by $\psi_{s,x_0}(x) = |s|^{-\frac{1}{2}}\psi(\frac{x-x_0}{s})$, and the * indicates the complex conjugate. For a mother wavelet, we choose the Morlet wavelet, $\psi(x) = e^{i2\pi nx}e^{-\frac{x^2}{2}}$, which is a sinusoid modulated by a Gaussian envelope. The parameter n controls the number of oscillations of the wavelet within the Gaussian envelope; we choose $n = 1$.

[14] The wavelet transform (1) is most efficiently calculated by using the Fourier transforms $\hat{p}(k)$ and $\hat{\psi}(k)$ of $p(x)$ and $\psi(x)$, respectively. Since our data (from both observations and the state estimate) are not uniformly spaced in the horizontal, we interpolate the data onto a uniform grid with spacing of 0.5 km before calculating Fourier transforms [*Cole et al.*, 2010]. Oversampling ensures that all resolved scales of variability are retained in the resulting wavelet transforms. Interpolated data are detrended by removing a linear least squares fit.

[15] The wavelet energy density in the (s, x_0) plane is $\frac{|\tilde{p}(s,x_0)|^2}{E_\psi|s|^2}$, where $E_\psi = \int_{-\infty}^{\infty}\frac{|\hat{\psi}(k)|^2}{|k|}dk$. The energy density is normalized such that its integral equals the sum of squared fluctuations from the linear least squares fit. For glider observations, we disregard energy content at wavelengths shorter than 6 km, the approximate Nyquist wavelength for glider observations every 3 km. The numerical simulation shows a decrease in energy content around 30-km wavelength due to resolution, so we only consider results from the simulation at scales larger than 30 km.

2.4. Passive Tracer Adjoint

[16] To investigate the sources of waters in layers defined by spice variability, we employ the passive tracer adjoint [*Fukumori et al.*, 2004; *Chhak and Di Lorenzo*, 2007; *Gao et al.*, 2011; *Song et al.*, 2011] in our state estimate. By integrating the passive tracer sensitivity backwards in time using the adjoint to the MITgcm [*Heimbach et al.*, 2005], we obtain the sensitivity of tracer concentration in a specified target region to tracer concentration at all previous locations and times in the model domain (see Appendix A). It is important to
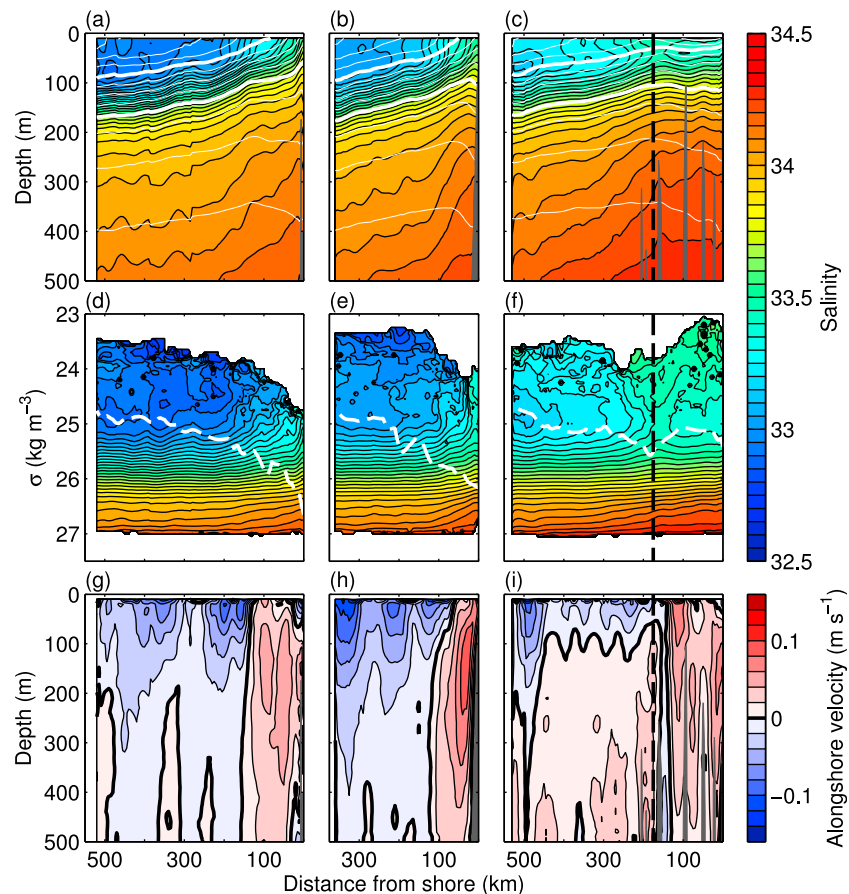
Figure 4. Observed (a–c) mean salinity (color) and density (white contours) on depth surfaces, (d–f) mean salinity on isopycnals, and (g–i) mean alongshore velocity from Line 66.7 (Figures 4a, 4d, and 4g), Line 80.0 (Figures 4b, 4e, and 4h), and Line 90.0 (Figures 4c, 4f, and 4i). In Figures 4a–4c, density contours are drawn every 0.25 kg m^{-3} with the 25.0 and 26.0 kg m^{-3} isopycnals bold. The dashed white lines in Figures 4d–4f indicate the densest outcropping isopycnal. Positive alongshore velocities are poleward. Bathymetry along the survey lines is shaded in Figures 4a–4c and 4g–4i. The dashed black lines in Figures 4c, 4f, and 4i indicate the Santa Rosa Ridge.

note that the passive tracer adjoint is not an inverse and does not allow us to track individual water parcels; it is impossible to "unmix" waters by inverting the numerical model since it is impossible to determine how to uniquely partition a water parcel into its constituents after mixing has taken place [*Fukumori et al.*, 2004]. In the adjoint model, advection runs backwards, but the diffusion operator is self-adjoint, meaning it operates as in a forward integration (see section A1).

[17] For each passive tracer, we create an objective function that represents tracer concentration averaged over the final six days of the simulation. The objective function J is given by

$$J = \int_{t_i}^{t_f} G[C(t), t] dt, \qquad (2)$$

where the function

$$G[C(t), t] = H[t - (t_f - T)] \iiint_V w(x, y, z) C(x, y, z, t) \, dx \, dy \, dz \qquad (3)$$

defines the target region. In (3), H is the Heaviside step function, t_f is the final time of the simulation, T is six days, $C(x, y, z, t)$ is the model tracer concentration in arbitrary units, V is the model domain, and $w(x, y, z)$ is a weight

function that defines the horizontal and vertical extent of the target region. The tracer sensitivity is $\partial J / \partial C(x, y, z, t)$ and evolves backwards in time according to the adjoint to the advection-diffusion equation (see section A2).

[18] When normalized by the total sensitivity over $t_f - T$ to t_f, the adjoint tracer sensitivity is the fraction of water in the target region at the end of the simulation that was located at (x, y, z, t); all sensitivities presented are normalized in this manner. Using the same numerical model that we are using, *Fukumori et al.* [2004] verified that the normalized adjoint tracer sensitivity can be interpreted as giving past distributions of tracers ending up in the specified target region by showing that the amount of passive tracer released from a source region that reached a specified target region in 1 year equaled the passive tracer adjoint sensitivity in the same source region with the same target region.

3. Results and Discussion

3.1. Large-Scale Structure

[19] Mean salinity and density as a function of depth (Figures 4a–4c) show the persistent, large-scale thermohaline
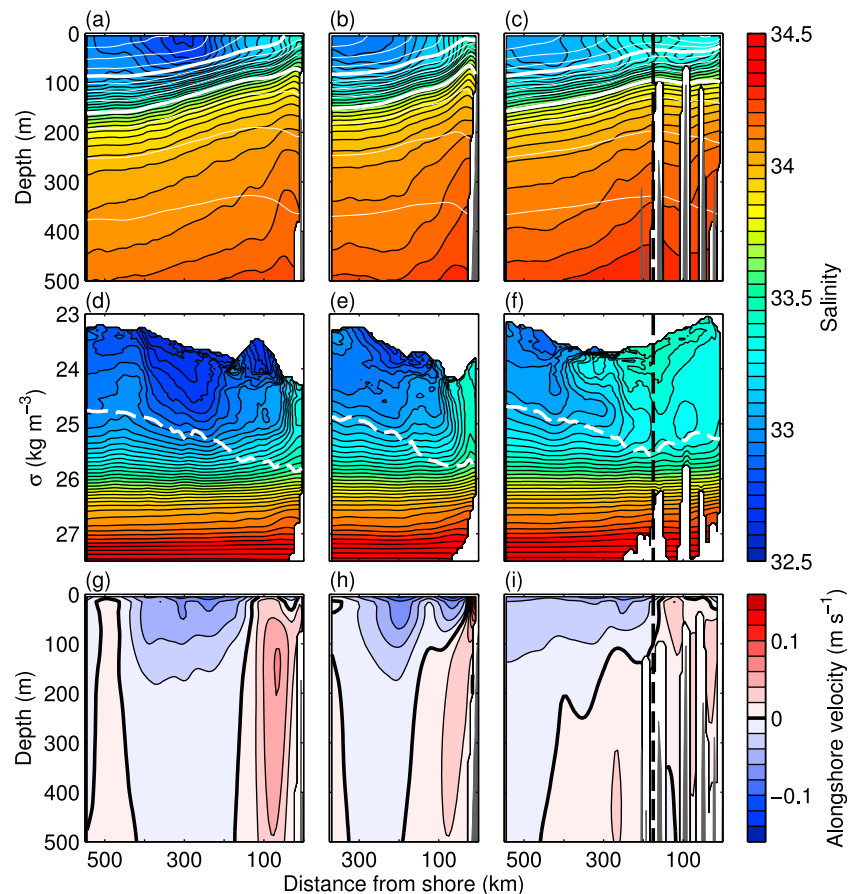
Figure 5. As in Figure 4 but for means in the numerical simulation from 1 January 2007 to 30 July 2009.

structure in the CCS. Low salinity above the pycnocline is the signature of the equatorward flowing California Current [*Lynn and Simpson*, 1987] with lowest salinity further offshore to the south. Near-surface salinity is greatest near the coast on Lines 66.7 and 80.0 and over the Santa Rosa Ridge on Line 90.0 due to upwelling of saltier thermocline waters [*Davis*, 2010]. Salinity increases with depth within and below the pycnocline. Deeper than 200 m, isohalines and isopycnals do not align; salinity increases along isopycnals toward the coast. This across-shore spice gradient is attributed to northward transport of subtropical waters by persistent poleward currents (Figures 4g–4i) [*Todd et al.*, 2011a].

[20] Mean salinity along isopycnals (Figures 4d–4f) has larger horizontal gradients along certain isopycnals. Above the densest outcropping isopycnal (the region we will refer to as the remnant mixed layer, following *Cole et al.* [2010]), large spice gradients near the coast on Lines 66.7 and 80.0 and over the Santa Rosa Ridge on Line 90.0 are, as above, the result of upwelling. Around the 26.0 kg m^{-3} isopycnal on all three lines, across-shore spice gradients are nearly zero. Below 26.5 kg m^{-3}, spice gradients increase again with the largest gradients collocated with the mean poleward currents (Figures 4g–4i) on each survey line.

[21] The presence of persistent, large-scale spice gradients provides a background gradient that can be stirred to produce thermohaline structure at smaller scales [*Klein and Hua*, 1990; *Ferrari and Rudnick*, 2000; *Ferrari and Polzin*, 2005]. The narrow poleward currents [*Todd et al.*, 2011a] adjacent to

similarly strong equatorward flows (Figures 4g–4i) create a horizontally sheared flow field that can stir the large-scale gradients to smaller scales. Subsequent stirring by eddies and other mesoscale features can then produce smaller-scale structure.

[22] Simulated mean salinity, density, and alongshore currents (Figure 5) over the 2.6 years of the state estimate capture the observed mean features well. Most importantly for this analysis, the simulation produces mean across-shore spice gradients that are largest in the remnant mixed layer and between the 26.5 kg m^{-3} and 27.0 kg m^{-3} isopycnals with a layer of small mean spice gradients around 26.0 kg m^{-3}. On an alongshore transect through the state estimate (Figure 1), mean properties show the alongshore structure that is not well-resolved by the glider observations (Figure 6). The low-salinity signature of the California Current is found in the upper 100 m and within the remnant mixed layer all along the transect with salinity decreasing toward the north. Below the pycnocline and remnant mixed layer, mean alongshore spice gradients (Figure 6b) are smaller than the corresponding across-shore gradients (Figures 5d–5f).

3.2. Mesoscale and Submesoscale Structure

[23] To show the mean thermohaline structure at smaller scales, we first integrate the wavelet transforms of observed along-isopycnal salinity across wavelengths of 30–200 km (which we refer to as mesoscales) and wavelengths of 6–30 km (which we refer to as submesoscales). The 30-km
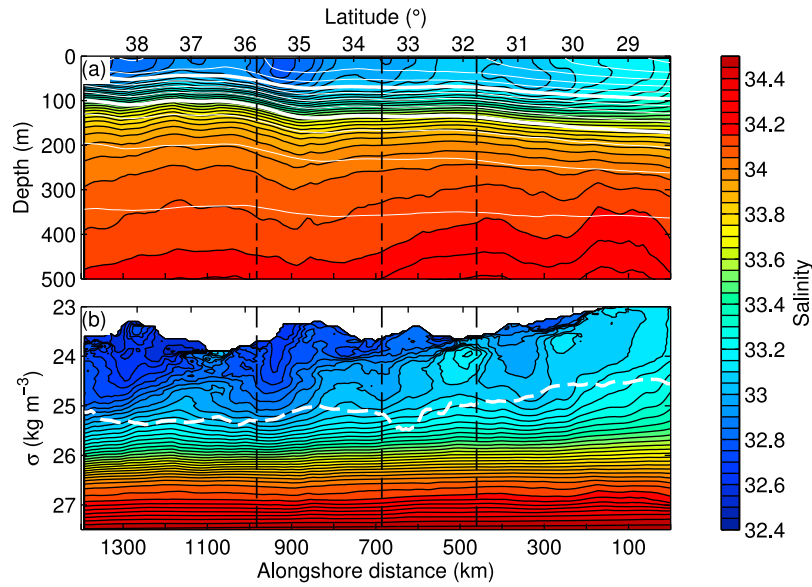
Figure 6. Mean salinity as a function of depth (a) and potential density (b) on the alongshore transect through the numerical simulation (Figure 1). Alongshore distance increases from south to north. White contours in Figure 6a show mean density with contours drawn every 0.25 kg m^{-3} and the 25.0 and 26.0 kg m^{-3} isopycnals bold. The dashed white line in Figure 6b indicates the densest outcropping isopycnal. Dashed black lines denote the intersections with Lines 66.7, 80.0, and 90.0 at station 80 along each line.

wavelength chosen to separate meso- and submesoscales corresponds to the first baroclinic Rossby radius in the area. We then average across the repeated transects to obtain the mean across-shore and vertical structure of spice variance at those scales (Figure 7). Along-isopycnal salinity had a k^{-2} spectrum on all isopycnals (not shown), consistent with previous observations [e.g., *Bernstein and White*, 1974; *Ferrari and Rudnick*, 2000; *Cole et al.*, 2010; *Cole and*
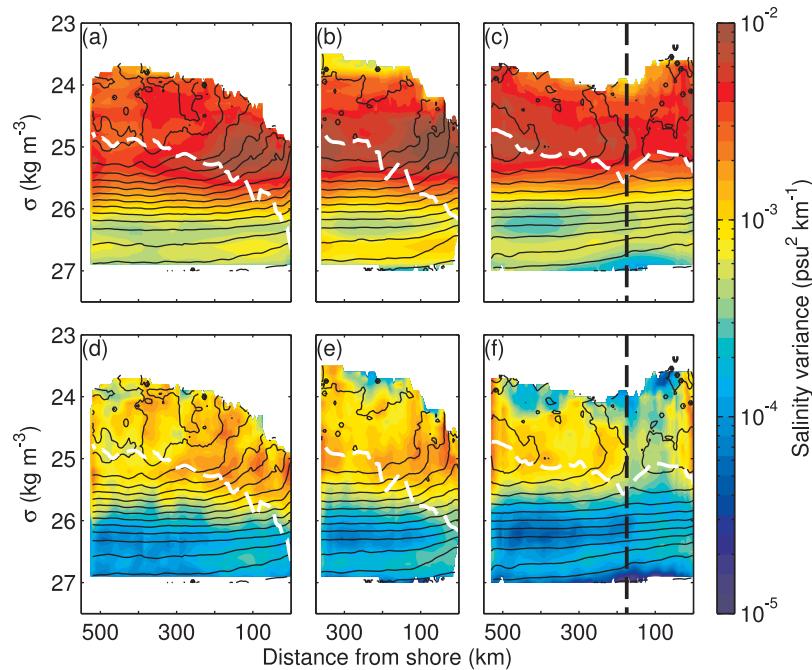
Figure 7. Observed (a–c) mesoscale (30–200 km wavelength) and (d–f) submesoscale (6–30 km wavelength) salinity variance along isopycnals as a function of density and across-shore distance on Line 66.7 (Figures 7a and 7d), Line 80.0 (Figures 7b and 7e), and Line 90.0 (Figures 7c and 7f). Black contours show mean salinity with a contour interval of 0.1. The dashed white lines indicate the densest outcropping isopycnal as in Figures 4d–4f. The dashed black lines in Figures 7c and 7f indicate the location of the Santa Rosa Ridge.
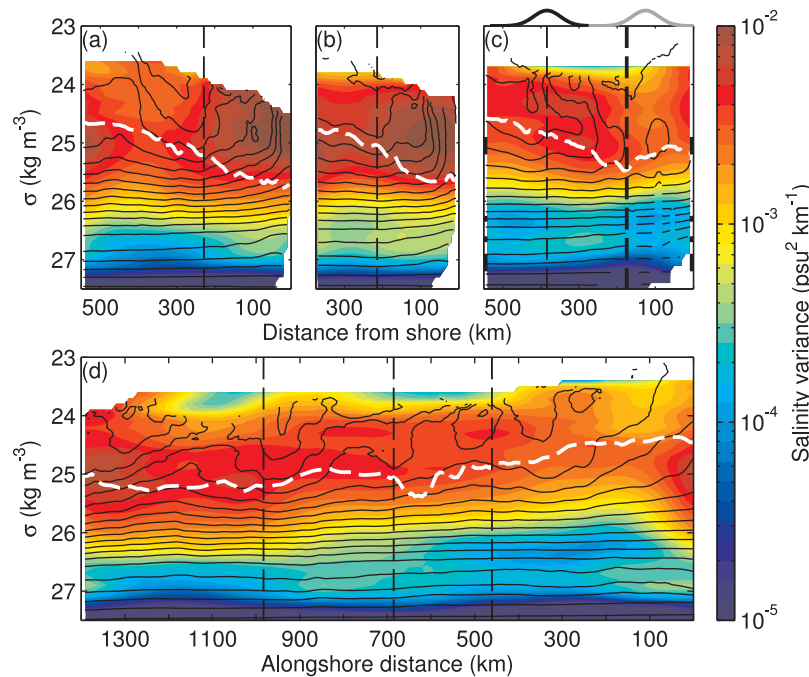
Figure 8. Mesoscale salinity variance along isopycnals as a function of density in the numerical simulation along Lines (a) 66.7, (b) 80.0, and (c) 90.0, for comparison to Figures 7a–7c and (d) along the alongshore transect shown in Figures 1 and 6. The dashed white lines indicate the densest outcropping isopycnals. The thin dashed lines in each panel indicate the intersections of Lines 66.7, 80.0, and 90.0 with the alongshore section. The heavy dashed line in Figure 8c indicates the Santa Rosa Ridge. Only mesoscale variance is shown because the model does not resolve submesoscales well. In Figure 8c, the Gaussian shapes on the top axis indicate the profile of the vertically integrated weight functions, w, for tracers with target regions offshore of the SCB (black) and within the SCB (grey), and the heavy marks along the vertical axes indicate the four density ranges used to define w for the along-isopycnal tracers (Table 1).

Rudnick, 2012] and simulations of stirring of thermohaline fronts [*Klein et al.*, 1998], so submesoscale spice variance was less than mesoscale spice variance at all locations. Since the individual wavelets have a constant quality factor Q, defined as the ratio of the wavelet's central frequency to its spread in frequency space [*Ferrari and Rudnick*, 2000], larger scales are less well-resolved spatially and mesoscale salinity variance (Figures 7a–7c) is smoother in the horizontal than the corresponding submesoscale salinity variance (Figures 7d–7f). The wavelet decomposition reveals three distinct along-isopycnal layers within the upper 500 m of the water column.

[24] Spice variance is highest within the remnant mixed layer at both mesoscales and submesoscales and along each survey line. This high spice variance is consistent with spice variance being set at the surface [*Cole et al.*, 2010]. In the across-shore direction, greatest spice variance within the remnant mixed layer is found 100–200 km offshore on Lines 66.7 and 80.0, where gradients of mean salinity are largest. On Line 90.0, largest spice variance within the remnant mixed layer is found just offshore of the Santa Rosa Ridge and 400–500 km from shore near the minimum in mean salinity (Figure 4f); spice variance decreases within the SCB in this layer, particularly at submesoscales (Figure 7f).

[25] Below the remnant mixed layer, spice variance decreases by more than an order of magnitude with increasing depth to a local minimum near 26.3 kg m^{-3} (Figure 7).

This minimum in meso- and submesoscale spice variance corresponds to the region with smallest mean large-scale spice gradient (Figures 4d–4f). Variance increases slightly toward shore in this layer along Lines 66.7 and 80.0. On Line 90.0, meso- and submesoscale spice variance increases significantly in this layer within the SCB, in contrast to the remnant mixed layer above (Figure 7).

[26] At densities of 26.6–26.7 kg m^{-3}, spice variance exhibits a local maximum on all three survey lines and at all observed scales. Spice variance in this layer is typically 3–5 times greater than in the minimum variance layer above but lower than in the remnant mixed layer. The density of this local maximum in spice variance corresponds to the isopycnals with largest mean salinity gradients below the thermocline (Figures 4d–4f). The maximum is apparent at all observed locations, but is generally strongest near the coast on each survey line. Similarities in cross-shore structure between the remnant mixed layer and deeper high variance layer (e.g., increased variance near the coast) may be a consequence of stirring by a velocity field that is often vertically coherent throughout the upper 500 m (e.g., Figures 4g–4i).

[27] The state estimate also shows layers defined by mesoscale spice variance (Figure 8). Along Lines 66.7, 80.0, and 90.0 (Figures 8a–8c), the state estimate has greatest spice variance in the remnant mixed layer and decreasing spice variance below 26.0 kg m^{-3}. A local minimum in spice variance near 26.3 kg m^{-3} is more apparent along Line

Table 1. Target Regions, Effective Horizontal Diffusivities κ_h, and Effective Diapycnal Diffusivities κ_v for Along-Isopycnal Passive Tracers

Tracer	Target Density (kg m^{-3})	Target Location	Spice Variance	κ_h[a] (10^2 m^2 s^{-1})	κ_v[a,b] (10^{-5} m^2 s^{-1})	κ_v[a,c] (10^{-5} m^2 s^{-1})
1-off	24.9–25.2	offshore SCB	high	12 ± 0.9	4.5 ± 0.1	3.8 ± 0.1
2-off	26.25–26.35	offshore SCB	low	9.8 ± 0.2	2.3 ± 0.1	2.1 ± 0.06
3-off	26.6–26.7	offshore SCB	high	6.4 ± 0.1	2.0 ± 0.02	2.1 ± 0.01
4-off	26.9–27.0	offshore SCB	low	2.6 ± 0.05	2.8 ± 0.01	2.8 ± 0.01
1-in	24.9–25.2	inshore SCB	high	11 ± 0.2	2.3 ± 0.06	2.0 ± 0.06
2-in	26.25–26.35	inshore SCB	low	7.6 ± 0.3	1.5 ± 0.03	1.7 ± 0.01
3-in	26.6–26.7	inshore SCB	high	2.8 ± 0.1	2.2 ± 0.04	1.9 ± 0.02
4-in	26.9–27.0	inshore SCB	low	1.6 ± 0.02	3.1 ± 0.03	3.1 ± 0.03

[a]Standard errors of diffusivities based on error estimates for the least squares fits [*Emery and Thomson*, 2004, p. 238] to the time series of second moments of tracer distributions (Figure 11).
[b]Here κ_v estimated from second moment relative to target isopycnal (Figure 15b).
[c]Here κ_v estimated from second moment relative to center of mass (Figure 15c).

90.0 than Line 80.0, and no local minimum is clear along Line 66.7. A local maximum in spice variance appears along Lines 80.0 and 90.0 near the 26.6 kg m^{-3} isopycnal, as in the observations. On Line 66.7, there is no clear local maximum near 26.6 kg m^{-3}, but spice variance at that density is highest near the coast as in the observations. The state estimate also produces layers of spice variance in areas not surveyed by the gliders and with little or no other in situ observations. Along CalCOFI Lines 73.3 (off San Simeon, California), 86.7 (off Los Angeles, California), and 93.3 (off San Diego, California), the simulation produces greatest spice variance in the remnant mixed layer, a local minimum in spice variance below the remnant mixed layer, and a local maximum in spice variance below 26.5 kg m^{-3} (not shown). The state estimate has a remarkable ability to accurately capture the geography of mesoscale spice variance by only adjusting initial conditions, boundary conditions, and forcing.

[28] Mean spice variance (Figure 8d) on the alongshore transect through the model domain (Figure 1) shows how the layers observed on each glider line are connected over the 525 km between Lines 66.7 and 90.0. Spice variance is greatest in the remnant mixed layer all along the 1400-km alongshore transect. The layer of minimum spice variance is most prominent south of Line 90.0 and becomes difficult to identify between Lines 80.0 and 66.7, consistent with observations. The deeper layer of increased spice variance near the 26.7 kg m^{-3} isopycnal can be traced from the southern boundary of the domain to near Line 66.7. Despite large-scale along-isopycnal salinity gradients being smaller in the alongshore direction (Figure 6b) than in the across-shore direction (Figures 5d–5f), mesoscale spice variance is of comparable size in the alongshore direction, possibly indicating that anisotropic large-scale gradients are ultimately stirred to produce isotropic mesoscale thermohaline structure.

3.3. Origin of Thermohaline Layers

[29] Layers with differing levels of thermohaline variance may form due to either differences in source waters or differences in stirring and diapycnal mixing between layers. Relevant source water characteristics include constituent water masses, which are related to large-scale thermohaline gradients (Figures 4d–4f), and small-scale spice variance set at the surface before subduction [*Cole and Rudnick*, 2012]. For similar background large-scale spice gradients on two layers, stronger stirring on one layer could produce greater

spice variance on that layer. Diapycnal mixing would tend to homogenize spice variance between layers.

[30] Passive tracer adjoint calculations (section 2.4) in the numerical state estimate allow us to investigate which of these mechanisms are responsible for the observed thermohaline structure in the CCS. We define eight along-isopycnal tracers that correspond to layers of high and low spice variance inshore and offshore of the SCB and 25 fixed-depth tracers offshore of the SCB. For each passive tracer, the weight function, w, in the objective function (equations (2)–(3)) defines the target region for that tracer. In all cases, the vertical integral of the weight function is Gaussian with an isotropic decay scale of 50 km. For along-isopycnal tracers, the distribution is centered at either CalCOFI station 90.80 (384 km offshore on Line 90.0, and the intersection with the alongshore transect of Figure 6) or CalCOFI station 90.45 (126 km offshore on Line 90.0); these locations are chosen because the layers are particularly distinct offshore of the SCB and spice variance within the SCB differs from other areas (Figures 7 and 8). The weight functions for along-isopycnal tracers are nonzero and constant in one of four density ranges corresponding to an identified layer of high or low spice variance (Table 1). In Figure 8c, the Gaussian shapes on the upper axis represent the vertical integral of w for tracers ending up inshore and offshore of the SCB, and the thick lines along the vertical axes represent the four density ranges. The 25 tracers that end up in specific vertical cells have target regions that are centered only at CalCOFI station 90.80 and defined for every other depth cell from the surface to about 1500 m. Since the along-isopycnal tracers best represent the layers of high and low spice variance, we primarily focus on their evolution; the fixed-depth tracers have greater vertical resolution and are used to better understand the changes in tracer movement with depth.

[31] Unrealistic negative tracer sensitivities appear as a result of known numerical errors in the adjoint model. Negative passive tracer sensitivities are unrealistic since they suggest that the presence of tracer in a particular location at a past time causes a decrease in concentration of that tracer in the target region at the end of the simulation. These negative sensitivities arise near sharp gradients of tracer where the third-order direct space-time advection scheme in the adjoint produces numerical errors. Our use of weight functions in equation (3) with vertical integrals that are Gaussian reduces horizontal gradients near the end of the simulation. However, the final vertical distributions do have sharp gradients
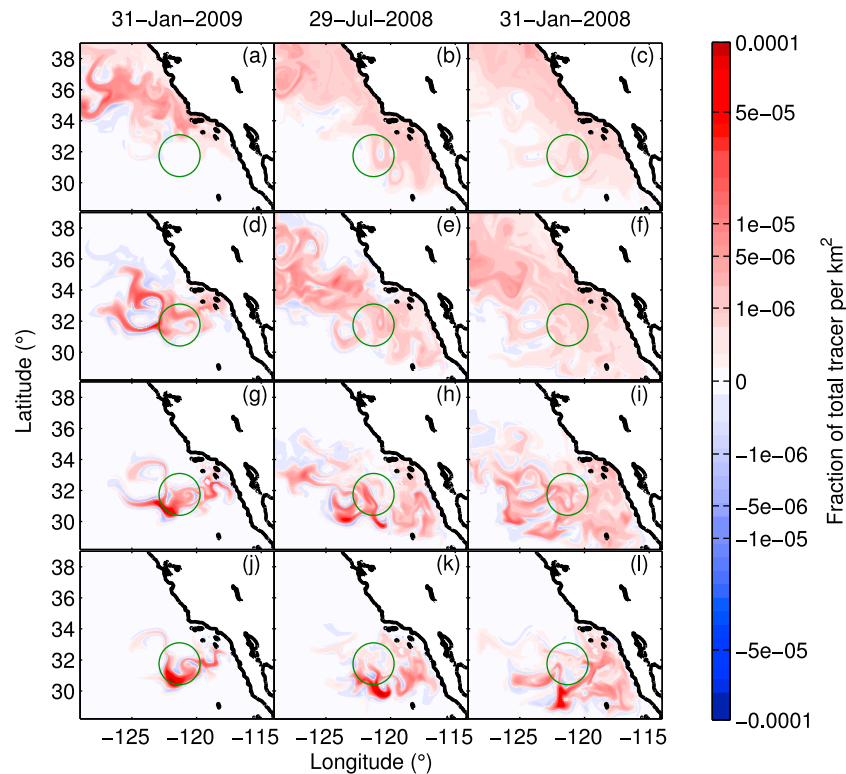
Figure 9. Snapshots of vertically integrated tracer distributions at (a, d, g, j) 6 months, (b, e, h, k) 1 year, and (c, f, i, l) 18 months before the end of the simulation for tracers 1-off (Figures 9a–9c), 2-off (Figures 9d–9f), 3-off (Figures 9g–9i), and 4-off (Figures 9j–9l). Total quantity is normalized by the amount on 24 July 2009. Green circles indicate the target region.

and straining by the velocity field tends to sharpen gradients as the adjoint model is integrated backwards in time. As is clear in Figures 9 and 10, which have symmetric, cube-root color scales, the negative values of vertically integrated sensitivities are much smaller than the positive values.

3.3.1. Snapshots of Tracer Distribution

[32] To characterize the horizontal distribution of the various tracers, we consider the vertically integrated tracer sensitivity, which we denote as $\tilde{C}(x, y, t)$. Figure 9 shows $\tilde{C}(x, y, t)$ for the four along-isopycnal tracers that end up offshore of the SCB 6 months, 1 year, and 18 months before the end of the simulation. Tracer 1-off (Figures 9a–9c), which represents the remnant mixed layer, is advected into the region primarily along the coast from the north, with some waters moving from 39°N to the target region within little more than 6 months. Waters in the low spice variance layer represented by tracer 2-off (Figures 9d–9f) are advected into the region more slowly and are found further offshore and to the south than the waters above; little of tracer 2-off is present along the coast north of Point Conception. Tracer 3-off (Figures 9g–9i), which represents waters in the high spice variance layer below the thermocline, comes into the region from the west and south with little tracer coming from north of Point Conception. The deeper, low spice variance waters of tracer 4-off arrive in the target region slowly from the south and within the SCB (Figures 9j–9l).

[33] Tracers found within the SCB at the end of the simulation have long term histories that are similar to those of

corresponding tracers that end up offshore of the SCB. Waters in the remnant mixed layer arrive in the SCB from the north along the coast (Figures 10a–10c). Tracers along deeper isopycnals (tracers 2-in, 3-in, and 4-in) enter the SCB primarily from the south due to the presence of the Santa Rosa Ridge (Figures 10d–10l). The distributions of tracers 2-in and 3-in 18 months before the end of the simulation (Figures 10f and 10i) resemble the distributions of tracers 2-off and 3-off, respectively, 1 year before the end of the simulation (Figures 9e and 9h) suggesting a timescale of about 6 months for waters to enter the SCB along those isopycnals. Waters along the deeper isopycnals represented by tracer 4-in are found along the coast for at least 18 months prior to the end of the simulation (Figures 10j–10l).

3.3.2. Mean Horizontal Movement

[34] We use the center of mass of the vertically integrated tracer sensitivity at each time step to characterize the mean movement of each tracer. Since the model has open boundaries, the tracers are not entirely within the model domain at all times and we can only calculate a sensible measure of the center of mass (and higher moments) when most of the tracer is within the model domain. To obtain the fraction of each tracer in the model domain as a function of time, we integrate the tracer sensitivity over the cropped domain at each time step (Figure 11a). For the final 6 months of the simulation, each of the along-isopycnal tracers is entirely within the cropped domain. Over the 2.6 year simulation, the shallowest tracers (tracers 1-off and 1-in) come most from outside of the cropped domain, while progressively deeper
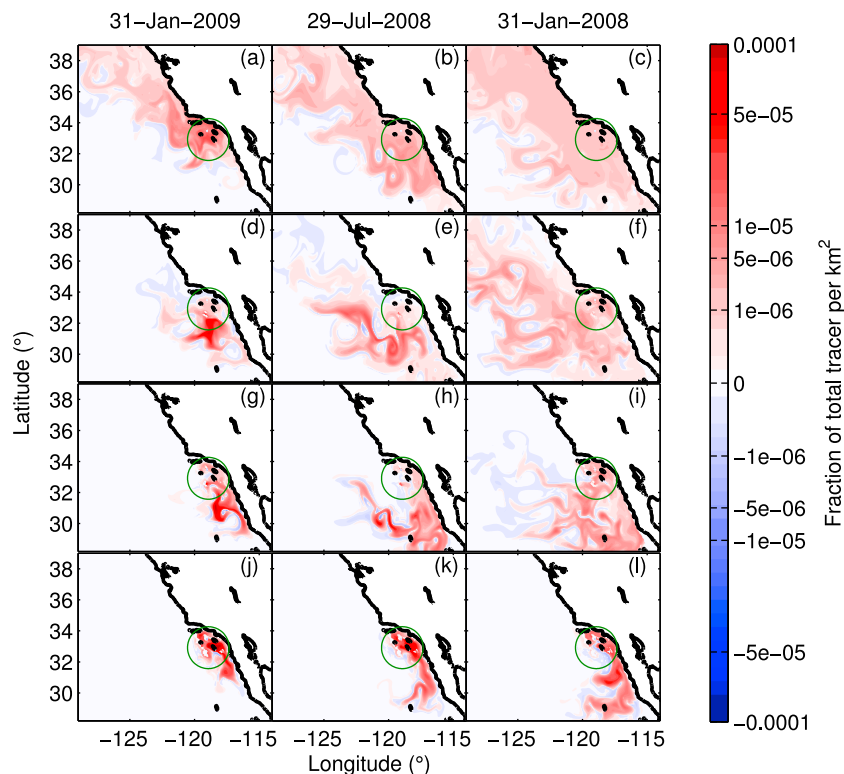
Figure 10. As in Figure 9 but for tracers (a–c) 1-in, (d–f) 2-in, (g–i) 3-in, and (j–l) 4-in.

tracers are more completely contained within the cropped domain throughout the simulation. Tracers 1-off and 1-in are the last tracers to be fully contained in the cropped domain, reflecting the influence of the surface-intensified California Current. Tracer 2-in is entirely within the cropped domain several months earlier than its offshore counterpart, tracer 2-off, reflecting the additional time required for waters to recirculate into the SCB [e.g., *Lynn and Simpson*, 1987]. Tracers 3-in and 4-in are found completely within the cropped domain slightly later than tracers 3-off and 4-off, and are slightly less completely within the domain at the beginning of the simulation than their offshore counterparts. This is likely a result of tracers 3-in and 4-in being advected northward more rapidly by the poleward currents (Figures 5g–5i) due to their target regions being closer to the coast. We will only calculate the center of mass (and higher moments) of the tracer distributions when 90% or more of the tracer is within the cropped domain.

[35] From the vertically integrated distributions of the along-isopycnal tracers at each time step (e.g., Figures 9 and 10), we calculate the center of mass, $(\bar{x}(t), \bar{y}(t))$, of each tracer as

$$\bar{x}(t) = \frac{\iint_{V'} x\tilde{C}(x,y,t)\,dx\,dy}{\iint_{V'} \tilde{C}(x,y,t)\,dx\,dy},$$

$$\bar{y}(t) = \frac{\iint_{V'} y\tilde{C}(x,y,t)\,dx\,dy}{\iint_{V'} \tilde{C}(x,y,t)\,dx\,dy},$$

(4)

where V' is the cropped model domain. The centers of mass of each tracer distribution (Figure 12) trace out the mean paths taken by waters that end up offshore and inshore of the SCB at the end of the simulation. As inferred from the snapshots of tracer distributions (Figure 9), waters in the remnant mixed layer (tracer 1-off) come into the region offshore of the SCB from the north along the coast, while the mean path of waters in the layer of minimum spice variance (tracer 2-off) is somewhat further offshore. The center of mass of tracer 3-off comes from primarily offshore reflecting advection from the northwest and southeast (Figures 9g–9i). Tracer 4-off reaches the target area offshore of the SCB from the most southerly location, but still shows some eastward motion in the early months of the simulation. The center of mass of tracer 1-in reaches the target region generally from the north but enters the SCB slightly to the south of its ultimate location. The centers of mass of progressively deeper tracers reach the target region in the SCB along trajectories that include increasingly long northward segments; the center of mass of tracer 4-in reaches the target region along a path that parallels the coast for more than 2 years. The Santa Rosa Ridge (Figure 1) serves as an increasingly solid barrier with increasing depth so that deeper tracers must enter the SCB primarily from the south.

[36] The along-isopycnal tracers clearly demonstrate a shift from northerly to southerly origin with increasing depth (Figure 12), but the minimal vertical resolution of those tracers (four tracers over about 500 m) leaves open the question of whether this transition occurs smoothly with increasing depth or abruptly with layers moving as discrete slabs. The paths of the centers of mass of the 25 tracers that
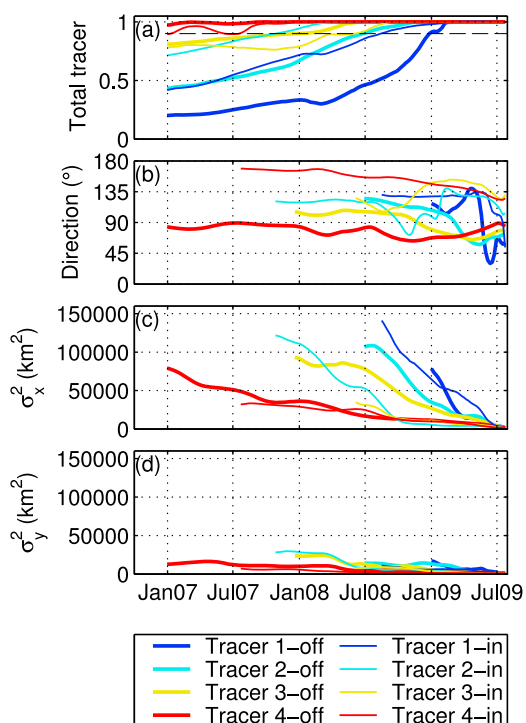
Figure 11. Time series of along-isopycnal tracer properties. (a) The fractional quantity of tracer within the cropped model domain is shown. Total quantity is normalized by the amount on 24 July 2009. The dashed black line indicates the threshold for calculating center of mass, angle of principal axes, and standard deviations along principal axes. (b) The orientation of the principal axes of the tracer distributions clockwise from north is also shown. (c, d) The variances of tracer distributions along the major and minor principal axes, respectively, are shown.

end up in specific depth cells, calculated using (4), provide information on the origin of waters with higher vertical resolution and allow us to show that the transition from northerly to southerly origin occurs abruptly with increasing depth.

[37] The paths of the centers of mass for the fixed-depth tracers (Figure 13a) can be sorted into three groups from the surface to 1500 m. From the surface to 155 m, tracers have northerly origins (blue shades in Figure 13); the northerly origin at these depths is consistent with mean southerly flow of the California Current in that depth range (Figure 5i). Tracers at depths from 200 to 750 m (red shades in Figure 13) have southerly origin, again consistent with mean currents. The centers of mass of tracers with target depths between 850 m and 1500 m (green shades in Figure 13) move little during the 2.6 year simulation, so their origin is unclear. Between the tracers with northerly and southerly origins, a single tracer with a target depth of 175 m (magenta in Figure 13) exhibits minimal mean displacement of its center of mass. Thus there are two layers with well-defined origins, one from the north and one from the south. Based on their northerly and southerly origins and depth ranges, these layers can be identified as Pacific Subarctic water (near-

surface) and Equatorial Pacific water (subsurface) [*Lynn and Simpson*, 1987]. Between the Pacific Subarctic and Equatorial Pacific water masses lies a thin layer with little mean displacement.
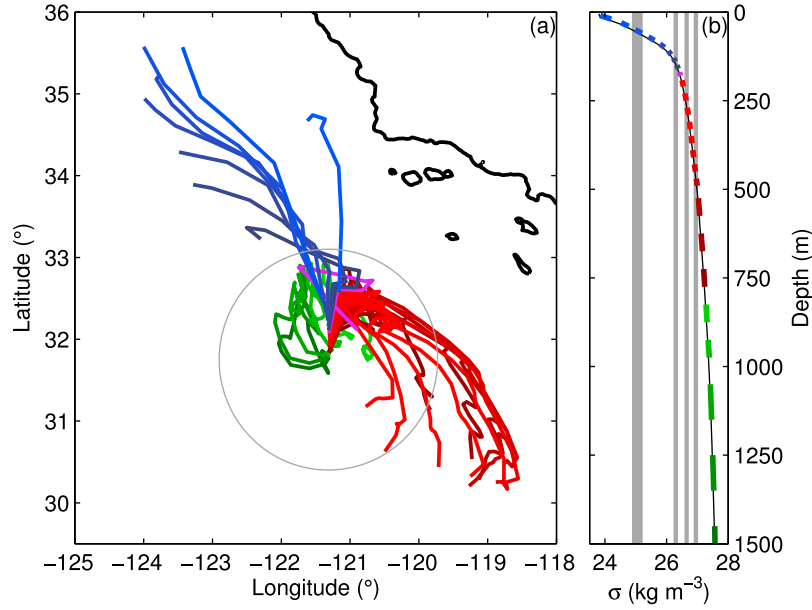
[38] The mean density profile in the target region at the end of the simulation (Figure 13b) allows us to identify where the layers of high and low spice variance, represented by the along-isopycnal tracers, are located relative to the water masses identified offshore of the SCB. Tracer 1-off is located in the middle of the layer of Pacific Subarctic water near 50 m depth, and, based on Figure 8c, the high spice variance remnant mixed layer generally coincides with this water mass of northerly origin. The deeper layer of high spice variance near the 26.6 kg m^{-3} isopycnal, represented by tracer 3-off, lies within the Equatorial Pacific water mass. The association of the deeper layer of high spice variance with Equatorial Pacific water is consistent with finding the layer extending from the southern boundary of the model domain to near Line 66.7 (Figure 8d). The minimum variance layer near the 26.2 kg m^{-3} isopycnal, however, lies in between the two water masses and near the level of the 175 m tracer (magenta in Figure 13) that showed little movement of its center of mass. The high spice variance layers are those that have distinct origins and correspond to named water masses. Between theses layers, diapycnal mixing between differing water masses can produce a layer of lower spice variance [see *Cole and Rudnick*, 2012].

3.3.3. Horizontal Dispersion

[39] To evaluate changes in stirring with depth as a possible mechanism for the generation of layers of high and low spice variance, we calculate variances of past distributions of along-isopycnal tracers and use those variances to estimate
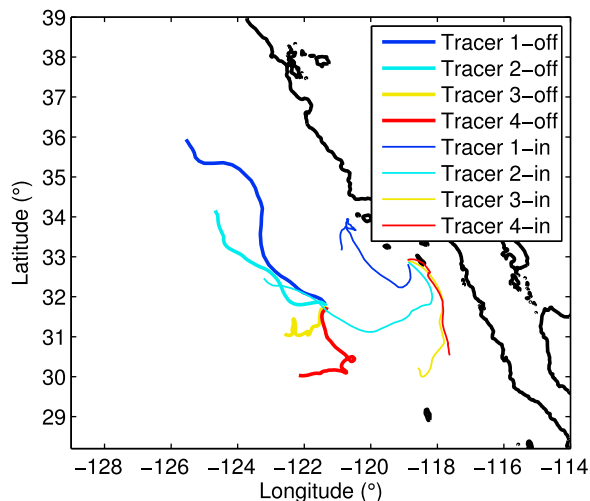
Figure 12. Location of center of mass of each along-isopycnal tracer. Tracers with target regions offshore of the SCB are shown with thick lines; tracers with target regions within the SCB are shown with dashed lines. Colors correspond to tracers along different isopycnal levels. The location of the center of mass is only shown when the amount of tracer in the cropped domain is at least 90% of the amount at the next to last time step (Figure 11a).

Figure 13. (a) Paths of the centers of mass of each of the fixed-depth tracers colored by depth range. The grey circle indicates the extent of the target region. (b) Mean potential density profile in the offshore target region at the end of the state estimate (black) with profiles at each model grid point weighted by the Gaussian function that defines the target region. Colored line segments denote the vertical ranges of the target regions for the 25 fixed-depth tracers. Grey bars indicate the density ranges used to define the along-isopycnal tracers in high and low spice variance layers. Colors correspond between Figures 13a and 13b.

the amount of horizontal dispersion within each layer. We first calculate the angle of the principal axes, $\alpha(t)$, as

$$\alpha(t) = \frac{1}{2} \arctan\left(\frac{2 \iint_{V'} x' y' \tilde{C}(x,y,t) \, dx \, dy}{\iint_{V'} (x'^2 - y'^2) \tilde{C}(x,y,t) \, dx \, dy} \right), \quad (5)$$

where $x' = x - \bar{x}(t)$ and $y' = y - \bar{y}(t)$ are distances from the center of mass at each time calculated on an f-plane centered at $(\bar{x}, \bar{y})$. Variances along the principal axes are then given by

$$\sigma_x^2(t) = \frac{\iint_{V'} x''^2 \tilde{C}(x,y,t) \, dx \, dy}{\iint_{V'} \tilde{C}(x,y,t) \, dx \, dy},$$

$$\sigma_y^2(t) = \frac{\iint_{V'} y''^2 \tilde{C}(x,y,t) \, dx \, dy}{\iint_{V'} \tilde{C}(x,y,t) \, dx \, dy}, \quad (6)$$

where distances from the center of mass along the principal axes, (x'', y''), are

$$\begin{pmatrix} x'' \\ y'' \end{pmatrix} = \begin{pmatrix} \cos\alpha & \sin\alpha \\ -\sin\alpha & \cos\alpha \end{pmatrix} \begin{pmatrix} x' \\ y' \end{pmatrix}. \quad (7)$$

[40] The orientation of the principal axes (Figure 11b) and variances along principal axes (Figures 11c and 11d) indicate how the past tracer distributions are spread about the center of mass at each time. Figure 14 shows ellipses representing the standard deviations along principal axes and centered at the center of mass as a function of time. With the

exception of tracer 4-off, each tracer has a major axis that is oriented southeastward for most of its history (Figure 11b), roughly aligning with the orientation of the coast (Figure 14) and alongshore currents. During the final months of the simulation, tracers 2-off, 3-off, and 4-off move toward the target region offshore of the SCB mainly in the across-shore direction (Figures 9d, 9g, and 9j), and the northeastward orientation of their principal axes near the end of the simulation (Figure 11b) reflects this motion. Possibly as a consequence of the slower alongshore flow at the depth of tracer 4-off, its principal axis remains oriented nearly perpendicular to the coast throughout the simulation (Figure 14g). Variance along the major axis is typically much larger than variance along the minor axis, indicating significant anisotropy in the past tracer distributions (Figures 11c and 11d). In the final months of the simulation, the orientation of the major axis for each tracer becomes poorly defined as the specified isotropic Gaussian distribution is obtained.

[41] As a measure of horizontal stirring and its dispersion of tracer, we calculate the growth rate of horizontal tracer variance [*Davis*, 1991]. We define an effective horizontal diffusivity, κ_h, as

$$\kappa_h = -\frac{1}{4} \frac{d}{dt} \left(\tilde{\sigma}_x^2(t) + \tilde{\sigma}_y^2(t) \right), \quad (8)$$

where $\tilde{\sigma}_x^2(t)$ and $\tilde{\sigma}_y^2(t)$ are linear least-squares fits to $\sigma_x^2(t)$ and $\sigma_y^2(t)$, and the minus sign accounts for the reversal of time in the adjoint model. Since the orientation of the principal axes changes with time, we calculate effective horizontal diffusivity based only on the total variance, though this does not account for the anisotropy of the past tracer distributions. The resulting horizontal diffusivities are given in Table 1.
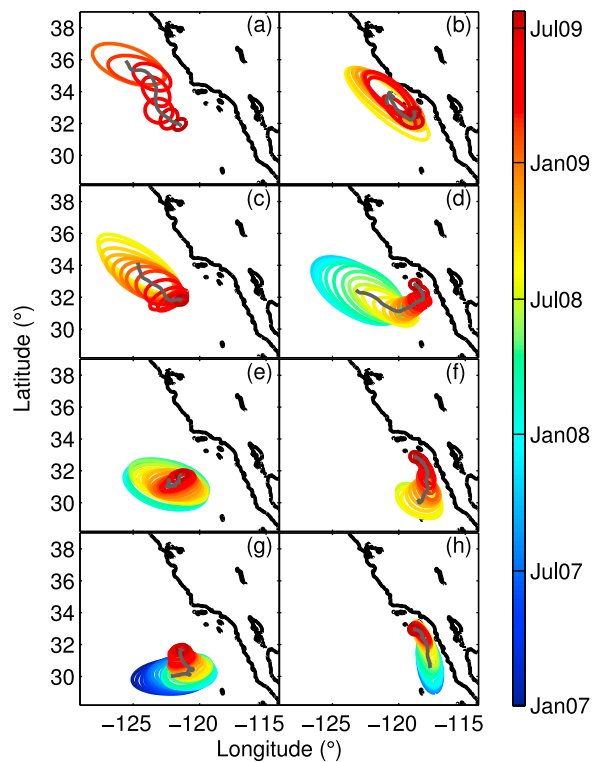
Figure 14. Variance ellipses for each along-isopycnal tracer as a function of time. (a, c, e, g) Tracers with target regions offshore of the SCB, from shallowest to deepest. (b, d, f, h) Tracers with target regions inshore of the SCB, from shallowest to deepest. Ellipses are centered at the center of mass and shown for tracer distributions every 30 days. The dark grey lines show the location of the center of mass as in Figure 12. Ellipses are shown only when the amount of tracer in the cropped domain is at least 90% of the amount at the next to last time step (Figure 11a).

Effective horizontal diffusivities decrease with depth for tracers ending up both inshore and offshore of the SCB. For each target density range, estimates of κ_h are smaller for tracers ending up within the SCB than for their offshore counterparts, consistent with increasing eddy scales as along-isopycnal distance from topography increases [cf. *Davis*, 1985, 1987]. This onshore-offshore contrast is most significant for the deepest tracers (Tracer 3-in/3-off and 4-in/4-off); movement of the inshore tracers in these density ranges is strongly affected by the presence of the Santa Rosa Ridge (section 3.3.2). The effective horizontal diffusivities from tracers 1-off and 1-in of 1.2×10^3 m^2 s^{-1} and 1.1×10^3 m^2 s^{-1}, respectively, are comparable to the apparent alongshore diffusivities reported from surface drifters off central California by *Davis* [1985] and the isopycnal eddy diffusivity calculated from tracer released in the pycnocline of the North Atlantic at scales of 300–1000 km [*Ledwell et al.*, 1998]. Apparent diffusivities are all much larger than the horizontal diffusivities of 1 m^2 s^{-1} used in the configuration of the numerical simulation. The dispersion of tracer in the model is significantly enhanced through straining by the velocity field. However, the monotonic decay of κ_h with depth suggests that variations in strength of

stirring with depth do not account for the observed layers of high and low spice variance.

3.3.4. Vertical Structure and Diapycnal Mixing

[42] To evaluate the influence of diapycnal mixing on the formation of layers of spice variance, we calculate effective diapyncal diffusivity, κ_v, from the three-dimensional fields of tracer sensitivity, which we treat as tracer distributions. Following *Ledwell et al.* [1993], we first calculate mean profiles of tracer sensitivity as a function of height above target isopycnal, $\hat{z}$, at each time step. We define the target isopycnal for each tracer to be the mean density in the target region during the final 6 days of the simulation, weighted by the function w in equation (3). The depth of the target isopycnal at each location and time, $z_0(x, y, t)$, is determined by linear interpolation of the simulated density field. We then define $\hat{z} = z - z_0(x, y, t)$. Individual profiles of tracer sensitivity are interpolated to a regular grid in $\hat{z}$ then averaged at each time step. The resulting mean profiles (e.g., Figure 15a, grey curves), show how tracer spreads vertically as time runs backwards in the adjoint model.

[43] Negative tracer sensitivities persist when profiles are averaged as a function of height above target isopycnal (e.g., Figure 15a). The numerical errors that produce these negative sensitivities occur where there are large gradients on the flanks of the tracer distribution, and these locations are aligned in height-above-target-isopycnal coordinates, so they are not canceled out by averaging all profiles at a given time step. Since the negative sensitivity values are unrealistic and cause problems when calculating moments of the vertical tracer distributions (e.g., negative variance), we fit Gaussians to the mean profiles at each time step using nonlinear least squares (e.g., Figure 15a, red curves). Downweighting negative sensitivities has little effect on the Gaussian fits. *Ledwell et al.* [1993] similarly fit Gaussians to means of observed tracer profiles in the ocean.

[44] Following *Ledwell et al.* [1993], we use time series of the second moments of our Gaussian fits to estimate effective diapycnal diffusivity, κ_v. The location of the center of mass of each tracer relative to the target isopycnal changes by a few 10s of m (not shown), but the finite thickness of our tracer distributions at the end of the simulation (a few 10s of m) and the vertical resolution of the model (10–20 m at the depths of the tracers) limits our ability to diagnose this mean diapycnal motion. So, like *Ledwell et al.* [1993], we calculate second moments relative to both the target isopycnal (Figure 15b) and the center of mass at each time step (Figure 15c). As for our estimates of κ_h, we make a linear fit, $\tilde{\sigma}_z^2(t)$, to the time series of second moments. From these fits, we estimate κ_v as

$$\kappa_v = -\frac{1}{2}\frac{d}{dt}\tilde{\sigma}_z^2(t), \qquad (9)$$

where, as in (8), the negative accounts for time reversal in the adjoint model.

[45] Estimates of κ_v are in the range of $1.5–4.5 \times 10^{-5}$ m^2 s^{-1} and do not depend strongly on which second moment is used in the estimate (Table 1). In all cases, the effective diapycnal diffusivity is higher than the value of 1×10^{-5} m^2 s^{-1} that is set explicitly in the model [*Todd et al.*, 2011a]. The largest estimates of κ_v are found in the remnant mixed layer offshore of the SCB (tracer 1-off), and can likely be
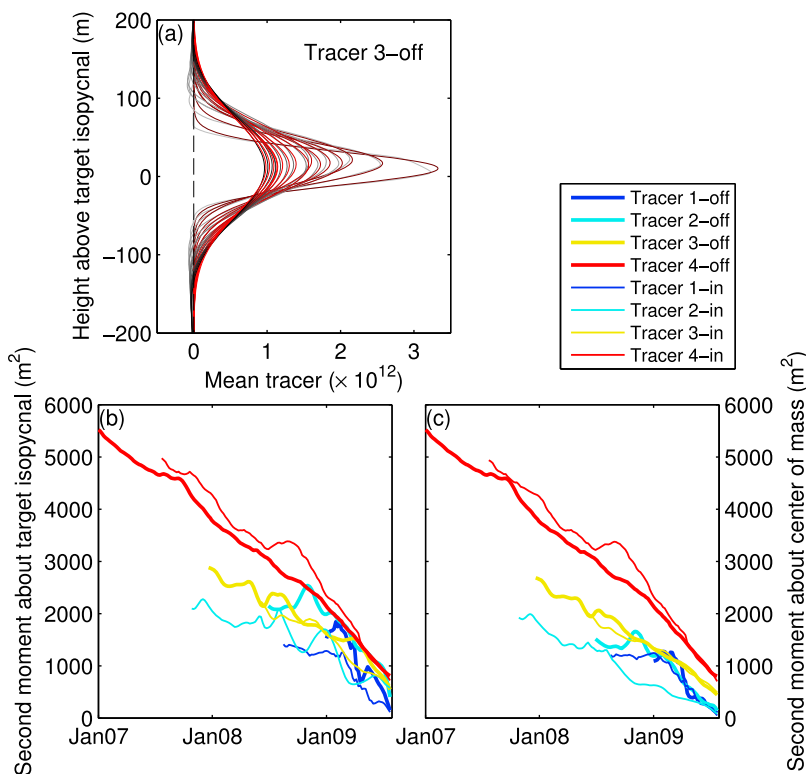
Figure 15. (a) Mean profiles of tracer sensitivity as a function of height above target isopycnal for Tracer 3-off (grey shades), and Gaussian fits to these mean profiles (red shades). Profiles are shown every 60 days with lighter greys and darker reds at later times. Time series of (b) second moment of mean tracer profiles about target isopycnal and (c) second moment of mean tracer profiles about the centers of mass. In Figures 15b and 15c, time series are shown only when 90% or more of the respective tracer is within the cropped model domain (Figure 11a).

attributed to interaction of the tracer with the surface mixed layer that is captured by the KPP mixing parameterization [*Large et al.*, 1994] in the model. Unlike κ_h, κ_v does not decrease monotonically with depth; after tracer 1-off, the next highest values of κ_v are found for tracers 4-in and 4-off, the deepest along-isopycnal tracers. This elevated diapycnal diffusivity at depth, particularly within the SCB, may reflect elevated mixing due to the currents interacting with the complex bathymetry of the SCB [cf. *Polzin et al.*, 1997]. Lowest estimates of κ_v are found in the low-spice-variance layer represented by tracers 2-off and 2-in and in the deeper high-spice-variance layer represented by tracers 3-off and 3-in. As with apparent horizontal diffusivities, the trends in effective diapycnal diffusivity cannot explain the formation of the layers of spice variance in the simulation and observations; if diapycnal mixing were the dominant mechanism creating the layers, we would expect to see high (low) values of κ_v in the low (high) spice variance layers since mixing destroys variability.

4. Conclusions

[46] We have used a combination of autonomous glider observations and a numerical state estimate to characterize upper ocean thermohaline structure in the CCS. With high spatial resolution and continuous occupation of defined survey lines, glider observations resolve thermohaline structure at mesoscales and submesoscales and show the presence of discrete layers distinguished by spice variance. The state estimate reproduces these features while obeying the model dynamics and, through passive tracer adjoint calculations, allows us to show that differing origins and histories of the layers lead to their unique thermohaline properties.

[47] Layers defined by spice variance are observed and modeled throughout the CCS (Figures 7 and 8). Highest spice variance at mesoscales and submesoscales occurs in the remnant mixed layer where waters have recently been in contact with the atmosphere. Around 26.3 kg m^{-3}, a local minimum in spice variance is found; the minimum is most prominent in the southern portion of the study region and offshore of the SCB. Near 26.6 kg m^{-3}, we find a local maximum in spice variance. The layers of high and low spice variance are found along isopycnals with large and small mean, large-scale spice gradients, respectively, suggesting that persistent, large-scale thermohaline gradients are stirred by the velocity field to produce smaller scale thermohaline structure. Layers defined by their spice variance were previously reported by *Cole and Rudnick* [2012] in the central north Pacific, so we expect that similar features will be found throughout the ocean as the necessary observations become available.

[48] Possible mechanisms responsible for the formation of layers defined by thermohaline variance are (1) differences in water masses, origin, and history of waters in each layer,

(2) differences in the strength of horizontal stirring between layers, and (3) changes in diapycnal mixing with depth. We use passive tracers in the adjoint to our numerical state estimate to investigate these mechanisms. Estimates of both effective horizontal diffusivity and effective diapycnal diffusivity indicate that straining by the velocity field enhances dispersion of tracer, but neither differences in horizontal stirring between layers nor changes in diapycnal mixing with depth are sufficient to explain the observed layers of high and low spice variance. We find that layers with high spice variance are those that have distinct origins and are associated with named water masses; mixing between layers leads to lower spice variance between the identified water masses. The layers of high spice variance in the remnant mixed layer and near 26.6 kg m^{-3} coincide with the Pacific Subarctic and Equatorial Pacific water masses, respectively; the intermediate layer of low spice variance and the region of low spice variance below 26.9 kg m^{-3} have little net movement (Figure 13).

[49] As a naturally occurring passive tracer [*Veronis*, 1972; *Cole and Rudnick*, 2012], spice is a useful and readily observable variable for inferring the history of waters. In this analysis, observations of spice reveal distinct layers between the mixed layer and 500 m depth throughout the CCS. However, we have only considered mean distribution of spice variance with no accounting of possible seasonal or longer term variability. The observational data set used here currently spans 4 years, so seasonal cycles are becoming reasonably well-resolved (Figure 2), and some interannual variability is apparent [e.g., *Todd et al.*, 2011b]. Investigation of seasonal and interannual variability in spice could reveal changes in circulation as well as stirring and mixing occurring on those timescales that could have important influences on the productivity of the rich ecosystem of the CCS.

Appendix A: Passive Tracer Adjoint

[50] Here we derive the evolution of the passive tracer sensitivity in the continuous framework. The adjoint to the advection diffusion equation that governs passive tracer evolution is derived in section A1, and section A2 derives the tracer sensitivity and shows that it obeys the adjoint to the advection diffusion equation. Other derivations exist in the references, particularly in discretized frameworks, but we present the derivation here for completeness and clarity.

A1. Adjoint to the Advection Diffusion Equation

[51] The concentration of a passive tracer, $C(x, y, z, t)$, evolves according to an advection-diffusion equation

$$\left(\frac{\partial}{\partial t} + \vec{u} \cdot \nabla - \kappa \nabla^2\right)C = 0. \quad (A1)$$

We consider an arbitrary variation δC to the tracer concentration. Since the advection-diffusion operator in (A1) is linear, the variation δC is also governed by an advection-diffusion equation

$$\left(\frac{\partial}{\partial t} + \vec{u} \cdot \nabla - \kappa \nabla^2\right)\delta C = 0. \quad (A2)$$

[52] We consider the inner product of (A2) with the adjoint variable $g(x, y, z, t)$. The adjoint variable is the solution to the adjoint differential equation that we are deriving. The form of $g(x, y, z, t)$ is found in section A2. We take the inner product of two fields to be the product of the two fields integrated over the domain, so we have

$$\int_{t_i}^{t_f} \int_0^X \int_0^Y \int_{-Z}^0 g\left(\frac{\partial}{\partial t} + \vec{u} \cdot \nabla - \kappa \nabla^2\right)\delta C \, dz \, dy \, dx \, dt = 0, \quad (A3)$$

where $[t_i, t_f] \times [0, X] \times [0, Y] \times [-Z, 0]$ is the model domain. The choice of the inner product is key to the definition of the adjoint operator.

[53] Green's identity [see *Lanczos*, 1961] states that for any linear differential operator, $\mathcal{L}$, we can find another uniquely determined operator, $\mathcal{L}^\dagger$, such that, for any pair of functions f and g that are sufficiently differentiable and satisfy appropriate boundary conditions

$$\int g\mathcal{L}f \, dx = \int f\mathcal{L}^\dagger g \, dx, \quad (A4)$$

when the definite integrals are extended over the entire domain. $\mathcal{L}^\dagger$ is the adjoint operator associated with $\mathcal{L}$, and g is the adjoint variable introduced previously. Applying Green's identity to (A3), we have

$$\int_{t_i}^{t_f} \int_0^X \int_0^Y \int_{-Z}^0 g\left(\frac{\partial}{\partial t} + \vec{u} \cdot \nabla - \kappa \nabla^2\right)\delta C \, dz \, dy \, dx \, dt$$
$$= \int_{t_i}^{t_f} \int_0^X \int_0^Y \int_{-Z}^0 \delta C\left(\frac{\partial}{\partial t} + \vec{u} \cdot \nabla - \kappa \nabla^2\right)^\dagger g \, dz \, dy \, dx \, dt$$
$$= 0. \quad (A5)$$

We proceed by integrating each term on the left hand side of (A5) by parts to obtain the form of the adjoint to the advection-diffusion operator.

[54] For the term with $\frac{\partial}{\partial t}$, we have

$$\int_{t_i}^{t_f} \int_0^X \int_0^Y \int_{-Z}^0 g\frac{\partial}{\partial t}\delta C \, dz \, dy \, dx \, dt$$
$$= \int_0^X \int_0^Y \int_{-Z}^0 \left[g\delta C|_{t_i}^{t_f} - \int_{t_i}^{t_f} \delta C\frac{\partial}{\partial t}g \, dt\right] dz \, dy \, dx$$
$$= \int_{t_i}^{t_f} \int_0^X \int_0^Y \int_{-Z}^0 \delta C\left(-\frac{\partial}{\partial t}\right)g \, dz \, dy \, dx \, dt, \quad (A6)$$

where the final equality holds if $\delta C|_{t=t_i} = g|_{t=t_f} = 0$ so that the boundary terms from the integration by parts vanish.

[55] For the part of the advective term with $\frac{\partial}{\partial x}$, we have

$$\int_{t_i}^{t_f} \int_0^X \int_0^Y \int_{-Z}^0 gu\frac{\partial}{\partial x}\delta C \, dz \, dy \, dx \, dt$$
$$= \int_{t_i}^{t_f} \int_0^Y \int_{-Z}^0 \left[gu\delta C|_0^X - \int_0^X \delta C\frac{\partial}{\partial x}(gu)dx\right] dz \, dy \, dt$$
$$= \int_{t_i}^{t_f} \int_0^X \int_0^Y \int_{-Z}^0 \left[\delta C\left(-u\frac{\partial}{\partial x}\right)g - \delta Cg\frac{\partial}{\partial x}u\right] dz \, dy \, dx \, dt$$
$$(A7)$$

if we require $g|_{x=0} = g|_{x=X} = 0$ so that the boundary terms vanish. The portions of the advective term in (A5) with

$\frac{\partial}{\partial y}$ and $\frac{\partial}{\partial z}$ give analogous results. The second term in the integrand of (A7) becomes part of a term with $\nabla \cdot \vec{u}$, which vanishes for incompressible fluids.

[56] For the diffusive term with $\frac{\partial^2}{\partial x^2}$, we apply integration by parts twice to get

$$\int_{t_i}^{t_f} \int_0^X \int_0^Y \int_{-Z}^0 g\left(-\kappa \frac{\partial^2}{\partial x^2}\right)\delta C \, dz \, dy \, dx \, dt$$
$$= \int_{t_i}^{t_f} \int_0^Y \int_{-Z}^0 \left[-g\kappa\frac{\partial}{\partial x}\delta C\Big|_0^X + \kappa\delta C\frac{\partial g}{\partial x}\Big|_0^X - \int_0^X \frac{\partial^2 g}{\partial x^2}\kappa\delta C \, dx\right] dz \, dy \, dt$$
$$= \int_{t_i}^{t_f} \int_0^X \int_0^Y \int_{-Z}^0 \delta C\left(-\kappa\frac{\partial^2}{\partial x^2}\right)g \, dz \, dy \, dx \, dt, \quad (A8)$$

where the final equality holds if we additionally require $\frac{\partial g}{\partial x}\big|_{x=0} = \frac{\partial g}{\partial x}\big|_{x=X} = 0$ so that the boundary terms vanish. The portions of the diffusive term in (A5) with $\frac{\partial^2}{\partial y^2}$ and $\frac{\partial^2}{\partial z^2}$ yield similar results. We see that the diffusion operator is self-adjoint.

[57] Collecting terms in (A6–A8) and their counterparts that are not shown and substituting into (A5), we have

$$\int_{t_i}^{t_f} \int_0^X \int_0^Y \int_{-Z}^0 \delta C\left(-\frac{\partial}{\partial t} - \vec{u}\cdot\nabla - \kappa\nabla^2\right)g \, dz \, dy \, dx \, dt$$
$$= \int_{t_i}^{t_f} \int_0^X \int_0^Y \int_{-Z}^0 \delta C\left(\frac{\partial}{\partial t} + \vec{u}\cdot\nabla - \kappa\nabla^2\right)^\dagger g \, dz \, dy \, dx \, dt.$$
$$(A9)$$

Since δC is arbitrary, the equality in (A9) holds only if the adjoint to the advection-diffusion operator is given by $-\frac{\partial}{\partial t} - \vec{u}\cdot\nabla - \kappa\nabla^2$. It follows that the adjoint variable g evolves according to

$$-\frac{\partial g}{\partial t} = \vec{u}\cdot\nabla g + \kappa\nabla^2 g, \quad (A10)$$

subject to $g|_{t=t_f} = 0$, $g|_\Omega = 0$, and $\hat{n}\cdot\nabla g|_\Omega = 0$, where Ω is the boundary of the domain and $\hat{n}$ is the unit vector normal to the boundary. The adjoint variable evolves backwards in time according to a velocity field that is oppositely directed relative to the forward equation, but diffusion continues to destroy gradients.

A2. Passive Tracer Sensitivity

[58] We now derive the sensitivity of passive tracer in a target region at the end of the simulation to tracer distributions at earlier times, and show that the passive tracer sensitivity is the adjoint variable g in section A1. Our derivation in the continuous framework closely follows the derivation by *Talagrand and Courtier* [1987] for variational assimilation. *Fukumori et al.* [2004] derive the passive tracer sensitivity in finite difference form.

[59] We write the advection-diffusion equation (A1) as $\frac{\partial C}{\partial t} = \mathcal{L}[C(t)]$, where $\mathcal{L} \equiv -\vec{u}\cdot\nabla + \kappa\nabla^2$ is now specified to be the advection-diffusion operator.

[60] We let $\langle,\rangle$ denote the inner product between two functions defined as the integral over the spatial domain of the product of the two functions. A variation $\delta C(t)$ to the

tracer concentration at time t results in a variation $\delta C(\tau)$ at each time $\tau > t$ to the tracer concentration. The resulting variation δJ to the objective function (2) is

$$\delta J = \int_t^{t_f} \left\langle \frac{\partial G}{\partial C}(\tau), \delta C(\tau)\right\rangle d\tau, \quad (A11)$$

where $\frac{\partial G}{\partial C}$ is the derivative of $G[C(t), t]$ with respect to $C(t)$ with x, y, z, and t held constant. As in section A1, the variation $\delta C(\tau)$ is governed by the advection-diffusion equation (A2). Solutions for $\delta C(\tau)$ can be written in terms of $\delta C(t)$ as

$$\delta C(\tau) = R(t, \tau)\delta C(t), \quad (A12)$$

where $R(t, \tau)$ is the resolvent of $\mathcal{L}$ from time t to time τ [see *Talagrand and Courtier*, 1987].

[61] Substituting (A12) into (A11) and applying Green's identity (A4) to the resulting inner product gives

$$\delta J = \int_t^{t_f} \left\langle [R(t,\tau)]^\dagger\frac{\partial G}{\partial C}(\tau), \delta C(t)\right\rangle d\tau. \quad (A13)$$

The application of Green's identity has removed the τ-dependent operator from $\delta C(t)$, which may now be written outside of the integral to give

$$\delta J = \left\langle \int_t^{t_f} [R(t,\tau)]^\dagger\frac{\partial G}{\partial C}(\tau)d\tau, \delta C(t)\right\rangle, \quad (A14)$$

from which we recognize that the sensitivity of the objective function with respect to tracer concentration at time t is

$$\frac{\partial J}{\partial C(t)} = \int_t^{t_f} [R(t,\tau)]^\dagger\frac{\partial G}{\partial C}(\tau)d\tau. \quad (A15)$$

[62] Now we recall the adjoint (A10) to the advection-diffusion equation that was derived in section A1, and we write it as

$$-\frac{\partial g}{\partial t} = \mathcal{L}^\dagger[g(t)], \quad (A16)$$

where $g(t)$ is the adjoint variable and $\mathcal{L}^\dagger$ is the adjoint of the operator $\mathcal{L}$, the form of which was derived in section A1. *Talagrand and Courtier* [1987] prove that the resolvent of the adjoint equation from time t_2 to time t_1 is the adjoint of the resolvent of the forward equation from time t_1 to time t_2. Therefore we can write (A15) as

$$\frac{\partial J}{\partial C(t)} = \int_t^{t_f} R^\dagger(\tau, t)\frac{\partial G}{\partial C}(\tau)d\tau, \quad (A17)$$

where $R^\dagger(\tau, t)$ is the resolvent of the adjoint operator $\mathcal{L}^\dagger$ backwards in time from τ to t.

[63] Now consider the inhomogeneous adjoint equation

$$-\frac{\partial g}{\partial t} = \mathcal{L}^\dagger[g(t)] + \frac{\partial G}{\partial C}(t), \quad (A18)$$

where the partial derivative of the function G that defines the objective function provides a forcing for the adjoint to the

advection-diffusion equation. The solution to (A18) subject to $g(t_f) = 0$ is

$$g(t) = \int_t^{t_f} R^\dagger(\tau, t) \frac{\partial G}{\partial C}(\tau) d\tau. \tag{A19}$$

We verify this solution by substitution and using the properties of the resolvent $R^\dagger$ that $R^\dagger(t, t) = I$ where I is the identity operator and $\frac{\partial}{\partial t} R^\dagger(t, t') = \mathcal{L}^\dagger R^\dagger(t, t')$ [*Talagrand and Courtier*, 1987]. Substituting (A19) into the left-hand-side of (A18) gives

$$
\begin{aligned}
-\frac{\partial g}{\partial t} &= -\frac{\partial}{\partial t} \int_t^{t_f} R^\dagger(\tau, t) \frac{\partial G}{\partial C}(\tau) d\tau \\
&= \int_t^{t_f} \mathcal{L}^\dagger R^\dagger(\tau, t) \frac{\partial G}{\partial C}(\tau) d\tau + R^\dagger(t, t) \frac{\partial G}{\partial C}(t) \\
&= \mathcal{L}^\dagger \underbrace{\int_t^{t_f} R^\dagger(\tau, t) \frac{\partial G}{\partial C}(\tau) d\tau}_{=g(t)} + \frac{\partial G}{\partial C}(t) \\
&= \mathcal{L}^\dagger [g(t)] + \frac{\partial G}{\partial C}(t).
\end{aligned} \tag{A20}
$$

[64] Since the expressions for $\frac{\partial J}{\partial C(t)}$ (A17) and $g(t)$ (A19) are the same, it follows that $\frac{\partial J}{\partial C(t)}$ is the adjoint variable $g(t)$. The passive tracer sensitivity is governed by the adjoint to the advection diffusion equation, and the sensitivity of J to prior tracer concentration is found by integrating the partial derivative of the function G backwards in time using the adjoint equation.

References

Bernstein, R. L., and W. B. White (1974), Time and length scales of baroclinic eddies in the central North Pacific Ocean, *J. Phys. Oceanogr.*, *4*, 613–624, doi:10.1175/1520-0485(1974)004<0613:TALSOB>2.0.CO;2.

Castelao, R., S. Glenn, and O. Schofield (2010), Temperature, salinity, and density variability in the central Middle Atlantic Bight, *J. Geophys. Res.*, *115*, C10005, doi:10.1029/2009JC006082.

Chhak, K., and E. Di Lorenzo (2007), Decadal variations in the California Current upwelling cells, *Geophys. Res. Lett.*, *34*, L14604, doi:10.1029/2007GL030203.

Cole, S. T., and D. L. Rudnick (2012), The spatial distribution and annual cycle of upper ocean thermohaline structure, *J. Geophys. Res.*, doi:10.1029/2011JC007033, in press.

Cole, S. T., D. L. Rudnick, and J. A. Colosi (2010), Seasonal evolution of upper-ocean horizontal structure and the remnant mixed layer, *J. Geophys. Res.*, *115*, C04012, doi:10.1029/2009JC005654.

Davis, R. E. (1985), Drifter observations of coastal surface currents during CODE: The statistical and dynamical views, *J. Geophys. Res.*, *90*(C3), 4756–4772.

Davis, R. E. (1987), Modeling eddy transport of passive tracers, *J. Mar. Res.*, *4*, 635–666.

Davis, R. E. (1991), Lagrangian ocean studies, *Annu. Rev. Fluid Mech.*, *23*, 43–64.

Davis, R. E. (2010), On the coastal-upwelling overturning cell, *J. Mar. Res.*, *68*, 369–385.

Davis, R. E., C. C. Eriksen, and C. P. Jones (2002), Autonomous bouyancy-driven underwater gliders, in *Technology and Applications of Autonomous Underwater Vehicles*, edited by G. Griffiths, pp. 37–58, Taylor and Francis, Philadelphia, Pa.

Davis, R. E., M. D. Ohman, D. L. Rudnick, J. T. Sherman, and B. A. Hodges (2008), Glider surveillence of physics and biology in the southern California Current System, *Limnol. Oceanogr.*, *53*(5–2), 2151–2168, doi:10.4319/lo.2008.53.5_part_2.2151.

Emery, W. J., and R. E. Thomson (2004), *Data Analysis Methods in Physical Oceanography*, 2nd ed., Elsevier, New York.

Ferrari, R., and K. L. Polzin (2005), Finescale structure of the *T–S* relation in the eastern North Atlantic, *J. Phys. Oceanogr.*, *35*, 1437–1454, doi:10.1175/JPO2763.1.

Ferrari, R., and D. L. Rudnick (2000), Thermohaline variability in the upper ocean, *J. Geophys. Res.*, *105*(C7), 16,857–16,883.

Fukumori, I., T. Lee, B. Cheng, and D. Menemenlis (2004), The origin, pathway, and destination of Niño-3 water estimated by a simulated passive tracer and its adjoint, *J. Phys. Oceanogr.*, *34*, 582–604.

Gao, S., T. Qu, and I. Fukumori (2011), Effects of mixing on the subduction of South Pacific waters identified by a simulated passive tracer and its adjoint, *Dyn. Atmos. Oceans*, *51*, 45–54, doi:10.1016/j.dynatmoce.2010.10.002.

Heimbach, P., C. Hill, and R. Giering (2005), An efficient exact adjoint of the parallel MIT General Circulation Model, generated via automatic differentiation, *Future Gener. Comput. Syst.*, *21*, 1356–1371, doi:10.1016/j.future.2004.11.010.

Hickey, B. M. (1979), The California Current System—Hypotheses and facts, *Prog. Oceanogr.*, *8*, 191–279.

Klein, P., and B. L. Hua (1990), The mesoscale variability of the sea surface temperature: An analytical and numerical model, *J. Mar. Res.*, *48*, 729–763.

Klein, P., A.-M. Treguier, and B. L. Hua (1998), Three-dimensional stirring of thermohaline fronts, *J. Mar. Res.*, *56*, 589–612, doi:10.1357/002224098765213595.

Lanczos, C. (1961), *Linear Differential Operators*, Van Nostrand, New York.

Large, W. G., J. C. McWilliams, and S. C. Doney (1994), Oceanic vertical mixing: A review and a model with a nonlocal boundary layer parameterization, *Rev. Geophys.*, *32*(4), 363–403, doi:10.1029/94RG01872.

Ledwell, J. R., A. J. Watson, and C. S. Law (1993), Evidence for slow mixing across the pycnocline from an open-ocean tracer-release experiment, *Nature*, *364*, 701–703.

Ledwell, J. R., A. J. Watson, and C. S. Law (1998), Mixing of a tracer in the pycnocline, *J. Geophys. Res.*, *103*, 21,499–21,529.

Lynn, R. J., and J. J. Simpson (1987), The California Current System: The seasonal variability of its physical characteristics, *J. Geophys. Res.*, *92*, 12,947–12,966.

Lynn, R. J., and J. J. Simpson (1990), The flow of the undercurrent over the continental borderland off southern California, *J. Geophys. Res.*, *95*, 12,995–13,008.

Marshall, J., C. Hill, L. Perelman, and A. Adcroft (1997a), Hydrostatic, quasi-hydrostatic, and nonhydrostatic ocean modeling, *J. Geophys. Res.*, *101*, 5733–5752.

Marshall, J., A. Adcroft, C. Hill, L. Perelman, and C. Heisey (1997b), A finite-volume, incompressible Navier Stokes model for studies of the ocean on parallel computers, *J. Geophys. Res.*, *102*, 5753–5766.

Munk, W. (1981), Internal waves and small-scale processes, in *Evolution of Physical Oceanography—Scientific Surveys in Honor of Henry Stommel*, edited by B. Warren and C. Wunsch, chap. 9, pp. 264–291, Mass. Inst. of Technol., Boston.

Perry, M. J., B. S. Sackmann, C. C. Eriksen, and C. M. Lee (2008), Seaglider observations of blooms and subsurface chlorophyll maxima off the Washington coast, *Limnol. Oceanogr.*, *53*(5–2), 2169–2179, doi:10.4319/lo.2008.53.5_part_2.2169.

Polzin, K. L., J. M. Toole, J. R. Ledwell, and R. W. Schmitt (1997), Spatial variability of turbulent mixing in the abyssal ocean, *Science*, *276*(5309), 93–96, doi:10.1126/science.276.5309.93.

Rudnick, D. L., and S. T. Cole (2011), On sampling the ocean using underwater gliders, *J. Geophys. Res.*, *116*, C08010, doi:10.1029/2010JC006849.

Rudnick, D. L., R. E. Davis, C. C. Eriksen, D. M. Fratantoni, and M. J. Perry (2004), Underwater gliders for ocean research, *Mar. Technol. Soc. J.*, *38*, 73–84.

Sherman, J., R. E. Davis, W. B. Owens, and J. Valdes (2001), The autonomous underwater glider "Spray", *IEEE J. Oceanic Eng.*, *26*(4), 437–446.

Song, H., A. J. Miller, B. D. Cornuelle, and E. Di Lorenzo (2011), Changes in upwelling and its water sources in the California Current System

driven by different wind forcing, *Dyn. Atmos. Oceans*, *52*(1–2), 170–191, doi:10.1016/j.dynatmoce.2011.03.001.

Talagrand, O., and P. Courtier (1987), Variational assimilation of meteorological observations with the adjoint vorticity equation. Part I: Theory, *Q. J. R. Meteorol. Soc.*, *113*, 1311–1328.

Todd, R. E., D. L. Rudnick, and R. E. Davis (2009), Monitoring the greater San Pedro Bay region using autonomous underwater gliders during fall of 2006, *J. Geophys. Res.*, *114*, C06001, doi:10.1029/2008JC005086.

Todd, R. E., D. L. Rudnick, M. R. Mazloff, R. E. Davis, and B. D. Cornuelle (2011a), Poleward flows in the southern California Current System: Glider observations and numerical simulation, *J. Geophys. Res.*, *116*, C02026, doi:10.1029/2010JC006536.

Todd, R. E., D. L. Rudnick, R. E. Davis, and M. D. Ohman (2011b), Underwater gliders reveal rapid arrival of El Niño effects off California's coast, *Geophys. Res. Lett.*, *38*, L03609, doi:10.1029/2010GL046376.

Torrence, C., and G. P. Compo (1998), A practical guide to wavelet analysis, *Bull. Am. Meteorol. Soc.*, *79*, 61–78.

Veronis, G. (1972), On properties of seawater defined by temperature, salinity, and pressure, *J. Mar. Res.*, *30*(2), 227–255.

Wunsch, C. (2006), *Discrete Inverse and State Estimation Problems With Geophysical Fluid Applications*, 371 pp., Cambridge Univ. Press, Cambridge, U. K.

Wunsch, C., and P. Heimbach (2007), Practical global oceanic state estimation, *Phys. D*, *230*, 197–208, doi:10.1016/j.physd.2006.09.040.

B. D. Cornuelle, R. E. Davis, M. R. Mazloff, and D. L. Rudnick, Scripps Institution of Oceanography, University of California, San Diego, 9500 Gilman Dr., La Jolla, CA 92093, USA. (bcornuelle@ucsd.edu; rdavis@ucsd.edu; mmazloff@ucsd.edu; drudnick@ucsd.edu)

R. E. Todd, Woods Hole Oceanographic Institution, 266 Woods Hole Rd., MS 21, Woods Hole, MA 02543, USA. (rtodd@whoi.edu)